Journal of Applied Fluid Mechanics, Vol. 18, No. 9, pp. 2349-2360, 2025.
Available online at www.jafmonline.net, ISSN 1735-3572, EISSN 1735-3645.
https://doi.org/10.47176/jafm.18.9.3263

Design and Flow Field Analysis of Extendable Leaching-optimized Cavern Construction Device for Salt Cavern Gas Storage

C. Zha[1], R. Pang[1†], W. Wang[1], J. Chen[2] and J. Zhao[2]

[1] *Beijing University of Technology, Beijing, 100124, China*
[2] *CNOOC EnerTech-Drilling & Production Co., Tianjin, 300452, China*

†*Corresponding Author Email: 2893228293@qq.com*

ABSTRACT

Salt cavern gas storage is one of the most important types of underground gas storage reservoirs. To address the inefficient initial cavern formation rates in solution mining-based gas storage facilities located within salt formations, an extendable leaching-optimized device for cavern construction has been designed. The device has three features: a controllable working status, an adaptable extension and a replaceable nozzle. Simulations employing FLUENT were conducted to analyze the hydrodynamic behavior surrounding the device, aligned with its working principles. Quantitative assessments revealed the coupled effects of three critical factors: nozzle inclination angle, flow injection velocity, and device rotational speed on the adjacent flow domain. Simulations demonstrated, first, that this device can alter the shape of the cavity by adopting positive circulation, and the turbulence formed by a nozzle angle of 0° is conical, which is the optimal angle for cavity construction; second, the higher the injection velocity, the greater the distance and width of the high-speed jet stream; third, rapid attenuation of jet propagation metrics (distance and width increments) occurred beyond critical velocity thresholds of 16 m/s; conclusively, angular velocity variations were identified as a dominant factor governing jet energy attenuation rates. This study provides a theoretical basis for the practical application of extendable leaching-optimized cavern construction device in the field.

Article History

Received November 24, 2024
Revised March 19, 2025
Accepted April 11, 2025
Available online July 5, 2025

Keywords:

Salt cavern
Solubilization devices
Salt cave dissolution technology
Rotating jet
Flow field simulation

1. INTRODUCTION

Currently, five types of underground natural gas storage are found globally: depleted oil reservoir and depleted gas reservoir storages, and aquifer, salt cavern, and cavern storages. Salt rock is renowned for its excellent properties, including low permeability, low porosity, excellent rheological properties, and water-soluble extraction, making it an internationally recognized optimal method for energy storage (Ding et al., 2015; Zong et al., 2023). Consequently, salt cavern underground reservoirs are extensively used for natural gas peak shaving (Yang et al., 2015) and strategic oil reserves (Niu et al., 2015). Salt rock, a prevalent type of sedimentary rock, exhibits outstanding self-healing capability, low permeability, and remarkable plasticity. The exceptional stability and minimal permeability of salt caverns broaden their applications beyond natural gas and oil storage to include compressed air energy storage, hydrogen and helium storage, and radioactive waste disposal (Shi et al., 2015). Additionally, they can participate in the peaking of various energy systems.

Currently, the single-well-vertical (SWV) construction method is the main method used for salt cavern construction (Yuan et al., 2021). This method achieves a completely vertical salt cavern via multistage leaching and is suitable for thick salt layers. However it is not only costly, but also has a long construction period (Jiang et al., 2019; Li et al., 2020). To expedite the construction of salt cavern gas storage, some researchers have proposed solutions. Liu et al. (2017) determined the construction process and shape of a two-well-horizontal (TWH) cavity through physical simulation tests and compared the feasibility of TWH and SWV cavity methods. The results indicated that the TWH cavity had better safety, higher flexibility, and lower cost than the SWV cavity. Jiang et al. (2016) conducted two model experiments using large-sized rock salt-moulded specimens and found that the construction rate in the two-well system was faster than that in the single-well system

NOMENCLATURE

SWV	Single-Well-Vertical	C_t	concentration of the rock salt solution at time t
TWH	Two-Well-Horizontal	δ	thickness of the boundary layer
A	dissolution area	*D*	diffusion coefficient
V	initial volume of the solution	ρ_s	density of rock salt
Q	flow rate	*R*	dissolved radius
C_s	saturated concentration of the rock salt solution	*T*	dissolution time

(1-3 pumping cycles). Li et al. (2023) adopted a small-spacing well-cavity method of formation using a large-sized cavity formation casing to discharge brine directly into the well. This had several advantages, including a fast rate of cavity formation, short construction period, and high rate of rock utilization. Ban et al. (2012) investigated expedited cavern development methodologies in salt formations, introducing innovative techniques such as parameter optimization strategies (e.g., brine injection rates and well configuration), borehole enlargement protocols, and dissolution-enhancing mechanical systems to accelerate leaching efficiency. Yuan et al. (2006) engineered a specialized apparatus tailored for initial leaching phases, demonstrating through field trials that mechanical acceleration during early-stage cavern generation achieved a leaching rate twice that of conventional methods.

Several researchers have conducted experimental analyses on the rates of dissolution and erosion of salt rocks. Jiang et al. (2012) performed controlled hydrodynamic experiments to identify dominant controls on salt dissolution kinetics. Their experimental data demonstrated a positive correlation between flow velocity (6-60 L/h) and halite dissolution rates, with measured values increasing from 0.58 $g \cdot cm^{-2} \cdot h^{-1}$ to 0.66 $g \cdot cm^{-2} \cdot h^{-1}$ across this velocity range. Durie and Jessen (1964) established foundational insights into flow regime effects, demonstrating that turbulent flow conditions (Re >4000) enhanced salt removal efficiency by 10–20 times relative to laminar flow (Re <2000). Zhang et al. (2022) quantified the impact of jet velocity on erosion efficiency, revealing that low-pressure submerged jets achieved a tenfold increase in salt erosion rates compared to static leaching methods. Their experimental data showed erosion mass loss rising from 10 $g \cdot min^{-1}$ to 20 $g \cdot min^{-1}$ as jet velocity increased from 25 $m \cdot s^{-1}$ to 50 $m \cdot s^{-1}$. Liu et al. (2015) employed a purpose-built recirculating dissolution reactor to probe brine chemistry-flow coupling effects, revealing that dissolution kinetics were governed by initial brine salinity gradients (50-200 g/L NaCl). Experimental results demonstrated flow rate dependency: 120 g of halite dissolved within 20 minutes at 50 L/h (360 g/h dissolution rate), compared to 40 minutes at 20 L/h (180 g/h). Zhang et al. (2017) found that the dissolution efficiency of jetting salt rock was more than 10 times higher than that of previous indoor leaching. Therefore, both the increased flow rate and turbulent flow state of the fluid in the salt cavern cavity can expedite dissolution of salt rock.

Based on the above research, to expedite the construction of salt cavern gas storage reservoirs, this study designed an extendable leaching-optimized device that can not only change the range of action of the fluid injected into the cavity, but also further change the fluid flow state inside the cavity through its own rotational motion. Hydrodynamic simulations of the device's peripheral flow domain were performed with FLUENT, guided by its operational mechanism and geometric configuration. The effects of injection velocity, rotational speed, and nozzle angle on cavity construction of the cavern were analyzed to optimize the parameter settings of the extendable leaching-optimized device. This study provides a theoretical basis for the practical application of extendable leaching-optimized devices in the field.

2. ENHANCING LEACHING EFFICIENCY IN PRIMARY CAVERN DEVELOPMENT FOR UNDERGROUND GAS STORAGE IN SALT FORMATIONS

2.1 Primary Cavity Development Based on the Extendable Leaching-Optimized Device

The SWV leaching process comprises two sequential operational stages: slotting phase and cavity-building phase, as defined by Zhao et al. (2003). The application of the extendable leaching-optimized device focuses on expediting the slotting phase to accelerate cavity formation. To address the technical challenges of layered salt rock formations, including thin evaporite strata, abundant argillaceous interbeds, and stringent brine salinity specifications, we developed an adaptive leaching process framework utilizing an extendable leaching-optimized device (Fig. 1).

Following the installation of the production casing and well cementation, conventional drilling tools were deployed to advance 10 m short of the salt formation base, thereby preventing unintended salt layer penetration. Subsequent to achieving target depth, the existing drilling assembly was modified by integrating a reaming bit to maximize the wellbore diameter. In accordance with Moditis et al. (2016), an intermediate tubular component was positioned within the borehole, coupled with direct fluid circulation for cavern development. Fresh water was injected into the salt caverns through the drill pipe, and high-concentration brine was sprayed onto the surface through the annulus between the drill pipe and outer tubes. Corrosion inhibitors (usually oil) the annular space between the production casing and outer pipe, promoting lateral development of salt caverns until the diameter of the cavity during the trenching phase reaches 0.5 m, as shown in Fig. 1 (a).

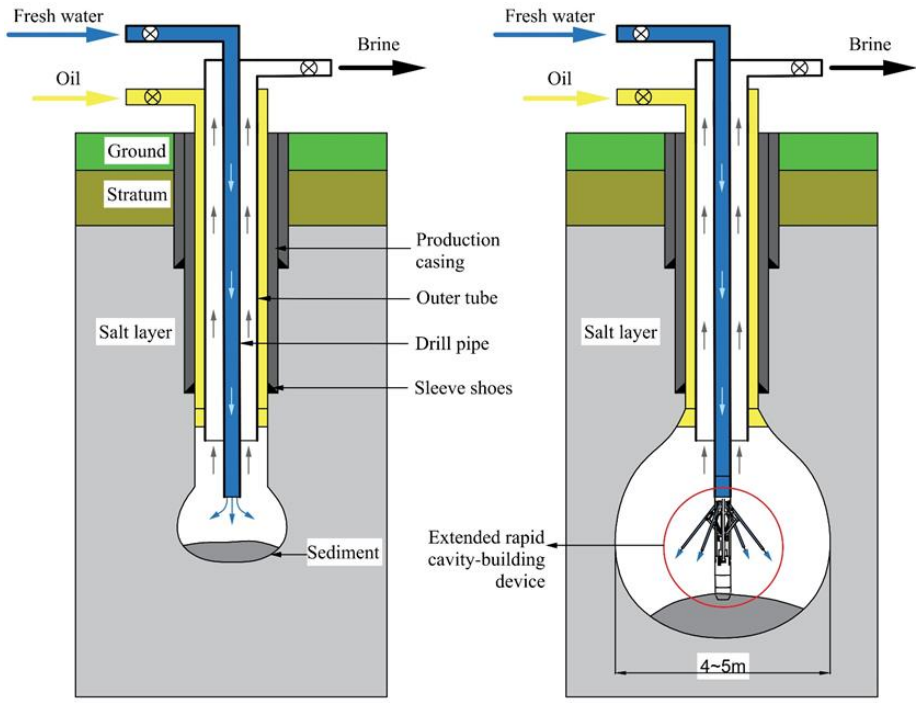

(a) (b)

Fig. 1 Dissolution construction process of a salt cavern gas storage device based on the extendable leaching-optimized device

The extendable leaching-optimized device was positioned at the cavity base and connected to the drill string, followed by high-pressure fluid injection upon achieving stable placement. Hydraulic actuation caused the device's high-pressure steel tubing to expand, while simultaneous rotation of the drill string facilitated progressive cavity enlargement. Upon attaining a cavern diameter of 4-5 m, the wellhead brine concentration achieved saturation, marking the transition to conventional leaching operations, as illustrated in Fig. 1 (b).

2.2 Structural Design of Extendable Leaching-Optimized Device

During the primary leaching phase of salt cavern development, the extendable leaching-optimized device significantly accelerates cavity enlargement, enabling efficient gas storage capacity creation. To achieve this functionality, a purpose-built extendable leaching-optimized device was engineered, with its design and operational principles comprehensively outlined in the following sections.

2.2.1 Structure of the Device

The structure of the extendable leaching-optimized device, which is mainly composed of a power structure, connecting rod structure, and supporting structure, is illustrated in Fig. 2. The power structure delivered both rotational and extensional forces to the device, incorporating a safety ejection mechanism. Hinged connections within the connecting rod structure enabled the deployment of high-pressure steel tubing, while the supporting structure maintained operational stability during cavity operations.

2.2.2 Principle of the Device

The power structure transferred rotational energy from the drill pipe to the device's upper end, while the supporting structure anchored the lower end to the accumulated insoluble residue via a guide shoe. During operation, high-pressure fluid was introduced into the drill pipe, with a portion diverted through the piston sleeve into the high-pressure tubing. This hydraulic pressure overcame spring resistance, driving the piston push rod downward and facilitating radial expansion of the high-pressure tubing via hinged connections. Through the meshing of the ratchet wheel of the upper face and the ratchet wheel of the lower cross-section, the power structure transmitted the rotating power to the connecting rod structure. The supporting shaft incorporated within the structural framework facilitated movement between the connecting rod assembly and the supporting components. Consequently, operational dynamics involved the power structure and connecting rod structure rotating independently of the stationary supporting structure.

2.3 Dissolution Capacity of the Device

2.3.1 Fluid Flow Velocity Influences the Dissolution of Salt Rocks

The dissolution performance of extendable leaching-optimized devices can be based on factors that affect the dissolution rate of salt rock. Yang et al. (2017) established an ordinary differential equation describing a special dissolution rate model of rock salt under a transient

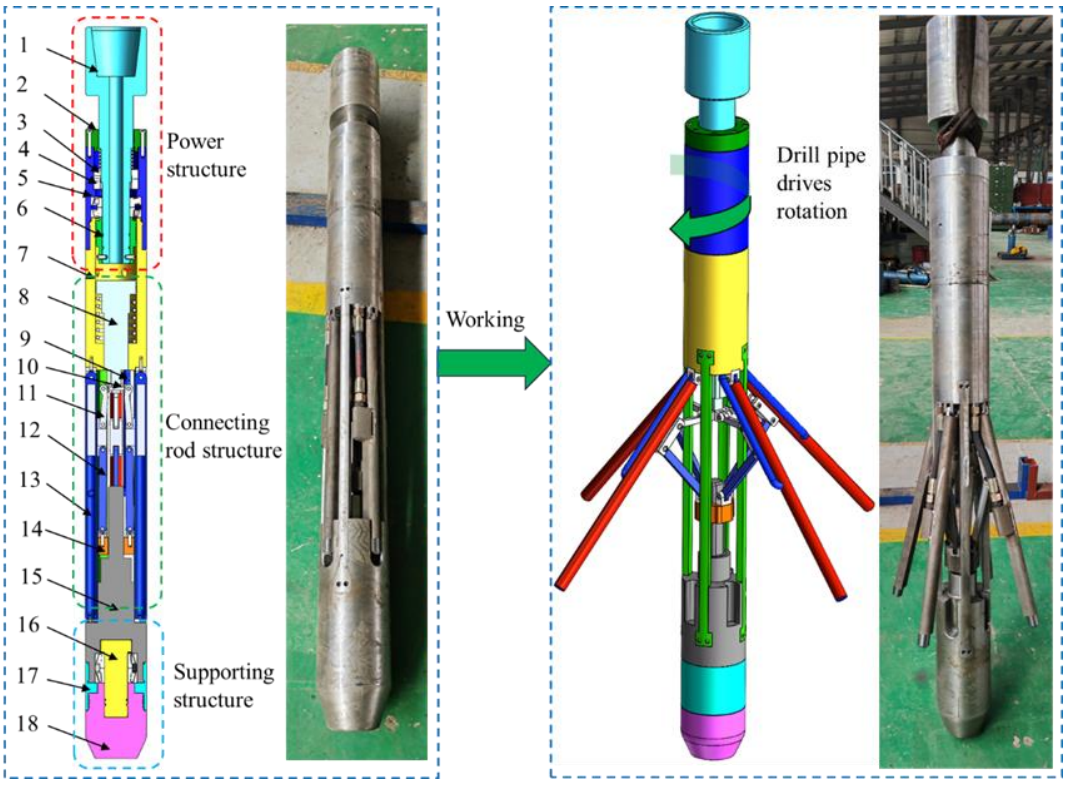

1—Suspension joint；2—Sealing cover；3—Upper face ratchet；4—Lower face ratchet 5—Suspension of the upper body；6—End cap；7—Piston sleeve；8—Piston push rod；9—High-pressure hose；10—Hinge support；11—Upper hinge rod；12—Lower hinge rod；13—High-pressure tubing；14—Restraint plate；15—Lower support short section；16—Supporting shaft；17—Lower bearing suspension；18—Guide shoe

Fig. 2 Schematic structure of extendable leaching-optimized device

diffusion process, involving calculation of the concentration distribution of rock salt solution at the boundary layer. Analytical solutions for the dissolution radius and solution concentration were obtained by mathematically solving an ordinary differential equation (Eq. (1)), and the relationship between the dissolution parameters of the analytical equation and the flow rate was explored (Eq. (2)):

$$\begin{cases} R = \dfrac{2DC_s}{\delta\rho_s}\dfrac{1}{2A\left(\frac{D}{\delta}\right)+Q}(V+Qt)\left[1-\left(\dfrac{V}{V+Qt}\right)^{1+\frac{2DA}{\delta Q}}\right] \\ C_t = C_s\dfrac{2AD}{\delta}\dfrac{1}{2A\left(\frac{D}{\delta}\right)+Q}\left[1-\left(\dfrac{V}{V+Qt}\right)^{1+\frac{2DA}{\delta Q}}\right] \end{cases} \tag{1}$$

$$\frac{D}{\delta} = 0.00437Q + 0.01427 \tag{2}$$

The dissolution kinetics of salt rock were strongly dependent on fluid flow velocity, with dissolution parameters demonstrating an approximately linear correlation with increasing flow rates. The velocity of the high-speed turbulence emitted by the device influenced the dissolution of the salt rock.

2.3.2 Fluid State Influences the Dissolution of Salt Rocks

Stiller et al. (2016) experimentally assessed the dissolution rates of natural halite in dilutions of Dead Sea (DS) brine, 10% to 90% by volume, under stirring and no-stirring conditions. At dilutions of 50% DS, dissolution rates were about two times larger than without stirring: at 10 minutes they were 13 mg/cm^2 min *versus* 5.8 mg/cm^2 min, respectively. Through a comprehensive investigation of turbulence dynamics, Wang et al. (2023) established a coupled multi-physics framework, demonstrating that turbulent flow enhances vortex generation, which subsequently alters saline concentration gradients. The primary feature of extendable leaching-optimized device is the generation of a wide range of turbulence (resulting from the turbulent circular jets of the nozzle and the rotation of the device to 'stir' the submerged fluid).

The dissolution performance of these devices can therefore be assessed based on the amount of turbulence generated.

The device existed in two states: stationary and rotating. When the device was stationary, the nozzle emitted a turbulent circular jet of fluid. When the device rotated, the turbulent circular jet at the nozzle was deflected by tangential forces, further altering the fluid state within the salt cavern. The axial flow velocity u_m and semi-extended thickness b of the jet are key parameters for assessing the effectiveness of turbulent circular jets. As the decay rate of u_m decreased, the growth rate of b in the jet increased, thereby expanding the effective range of the turbulent circular jet. The assumption that the turbulence is a 'free turbulent jet', as depicted in Fig. 3, was supported by experimental findings (Albertson et al., 1950):

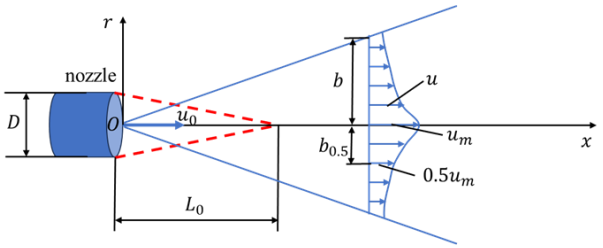

Fig. 3 Schematic diagram of a free turbulent circular jet

$$b = 0.25x \tag{3}$$

$$\frac{u_m}{u_0} = \frac{6.2D}{x} \tag{4}$$

3. NUMERICAL SIMULATION

3.1 Numerical Simulation Domain and Grid Construction

Guided by the functional mechanisms detailed in Section 2.2, pressurized hydraulic fluid entered the device through an articulated connector and was subsequently discharged into the salt cavern through jet orifices. To assess the leaching efficacy of the system — governed by turbulence intensity distributions during operation — hydrodynamic simulations of the ambient flow field were performed, as visualized in Fig. 4. A cylindrical computational fluid domain with vertical and cross-sectional dimensions of 5 m and 3 m respectively was established, segmented into two designated fluid regions (fluid-1 and fluid-2). The numerical model incorporated the following assumptions: (1) Flow behavior inside the device was excluded from the analysis; (2) equalized fluid ejection rates were assumed for all four jet orifices; and (3) the device's geometric configuration was simplified to a cylindrical profile, minimizing external flow disturbances caused by surface irregularities. A monitoring point at coordinates '0.7 m, 0 m, -0.6233 m' within fluid-1 was designated for grid independence verification. A hybrid meshing strategy was used to balance computational efficiency and accuracy; refined tetrahedral elements resolved high-velocity gradients near rotational regions, whereas coarse hexahedral elements discretized peripheral zones with attenuated flow interactions. The mesh independence verification was conducted under the conditions of an injection velocity of 16 m/s, rotational speed of 180RPM, and nozzle angle of 0°. The simulation was transient, and the velocity of the monitoring point stabilized after 4s. Four mesh precision ratio models in fluid-1 were selected for mesh-independence verification. The velocity of the monitoring point after 4s varied with the number of mesh elements, as listed in Table 1. Using Case 4 as a reference, when the number of mesh elements was reduced by half, the error increased by 2.47%. Considering the computational conditions, a mesh model with 2779327 elements in Case 3 was selected for subsequent research.

3.2 Boundary Conditions

As derived from the operational principles of the device, the injection velocity of the turbulent circular jet, the rotational speed of the device, and the nozzle angle collectively govern the turbulence intensity within the external flow field. Consequently, these parameters — injection velocity (defining injection boundary conditions), rotational speed, and nozzle angle (influencing model selection) — were selected as the critical variables. Figure 5 illustrates the geometric configurations of the three nozzle angles. To address the rotational motion of the device, a sliding mesh approach was implemented, in which varying rotational speeds dictated the mesh dynamics

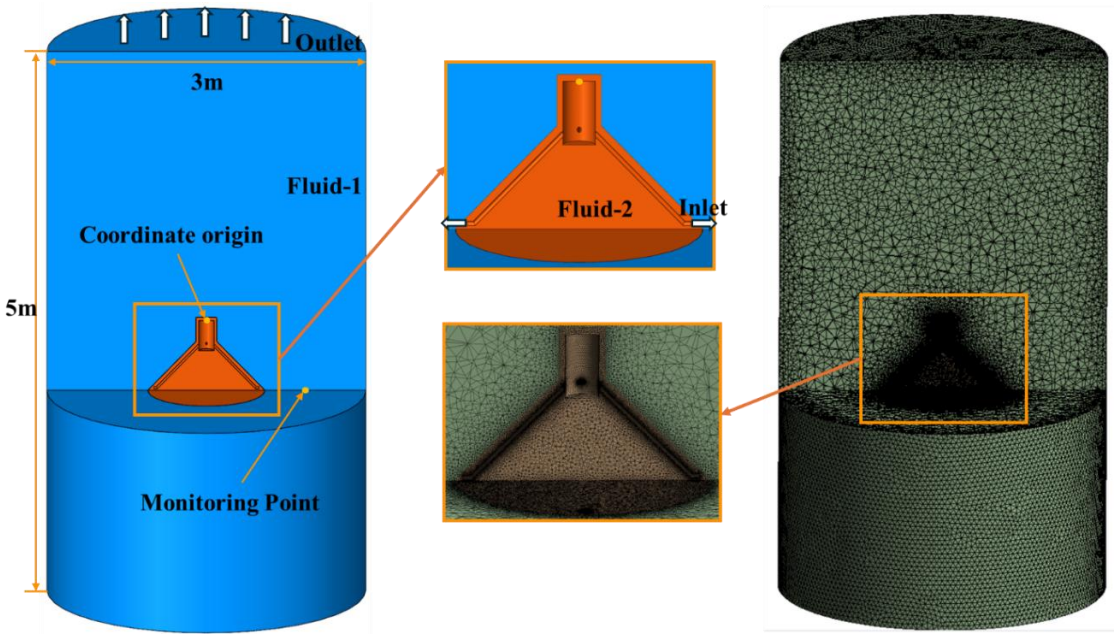

Fig. 4 Computational fluid domain and meshing in the simulations

Table 1 Grid independence verification

Example	Size of grid (mm)	Number of grid points	Velocity at the monitoring point (m/s)	Error
Case 1	150	2132310	0.87893	17.89%
Case 2	100	2216856	0.88408	17.4%
Case 3	50	2779327	1.04407	2.47%
Case 4	20	4020695	1.07046	0

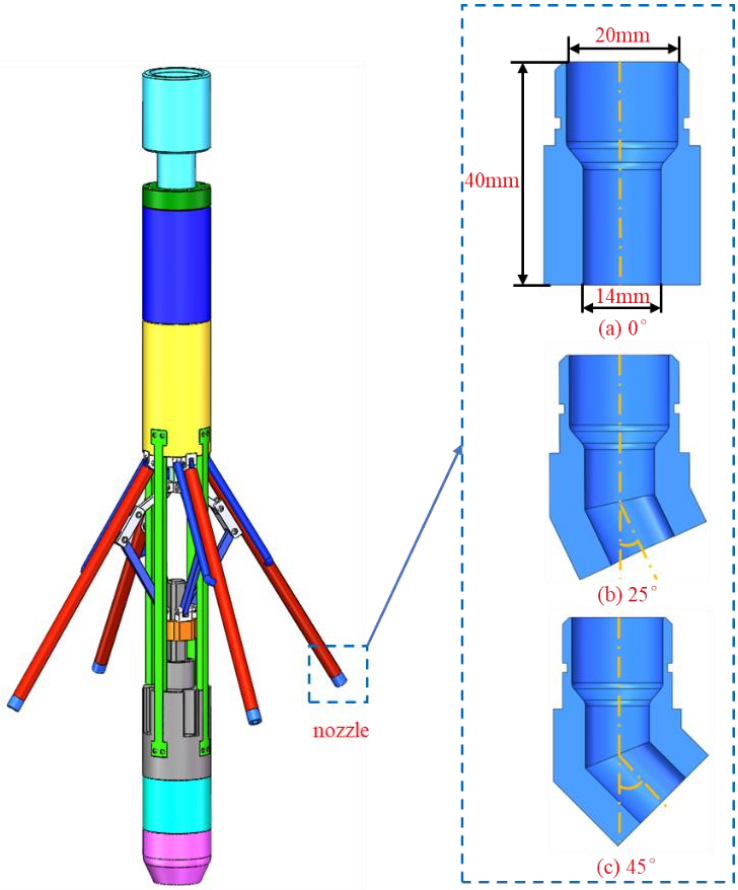

Fig. 5 Modeling of three different nozzle angles

Table 2 Boundary conditions

Nozzle inclination angle	Item	Classification	Value
0°	Inlet	Injection velocity	8 m/s, 12 m/s, 16 m/s, 20 m/s
	Outlet	Outlet pressure	0.1 MPa
	Cell zone conditions	No-slip surface conditions	
0°	Inlet	Injection velocity	16 m/s
	Outlet	Outlet pressure	0.1 MPa
	Cell zone conditions	Mesh motion	10 RPM, 30 RPM, 60 RPM, 120 RPM, 180RPM
25°	Inlet	Injection velocity	16 m/s
	Outlet	Outlet pressure	0.1 MPa
	Cell zone conditions	Mesh motion	180RPM
45°	Inlet	Injection velocity	16 m/s
	Outlet	Outlet pressure	0.1 MPa
	Cell zone conditions	Mesh motion	180RPM

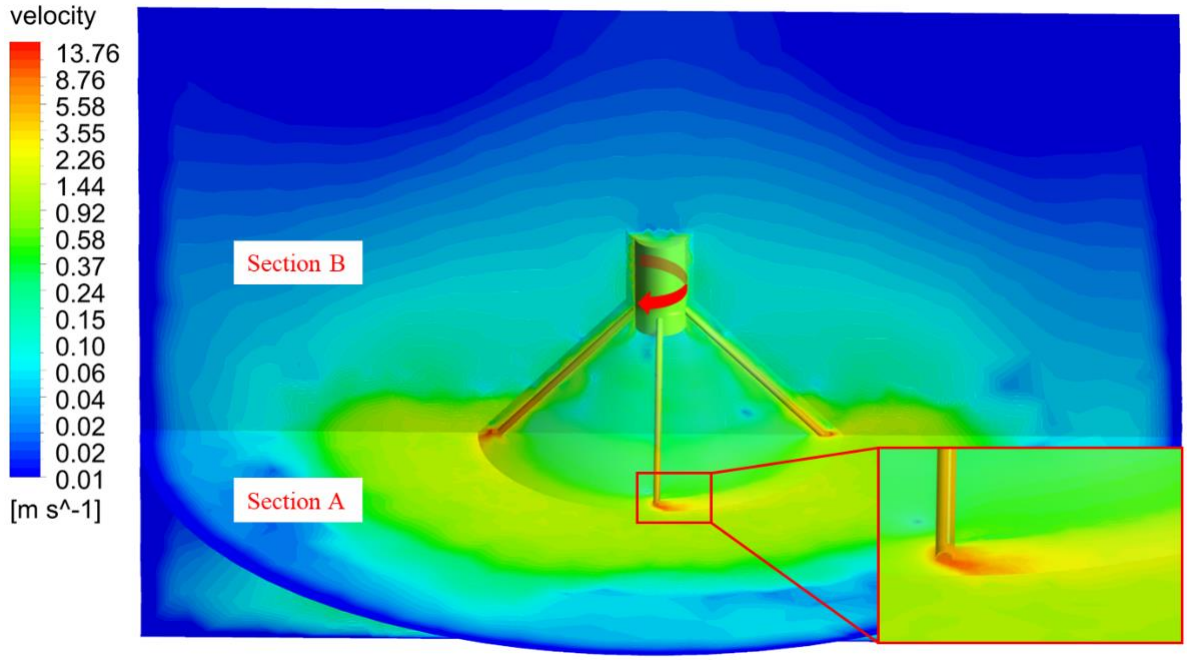

Fig. 6 The influence of device rotation on external flow field

within the cell zones. The detailed boundary conditions, including pressure, turbulence, and wall treatments, are summarized in Table 2.

3.3 Mathematical Formulations and Turbulent Flow Modeling

The fluid injection was designed as a circular jet. For the inlet condition of 8 m/s velocity and 14 mm circular diameter, the Reynolds number calculation followed Eq. (5):

$$Re = \frac{\rho v D}{\mu} \tag{5}$$

yielding a Reynolds number of 112,000 at the injection, indicating strong turbulent flow. Compared to the standard k – ε model, the Realizable k - ε model has been demonstrated to provide superior accuracy in predicting dissipation rate distributions for both planar and circular jets (Shaheed et al., 2019). The Realizable k – ε turbulence model exhibits significant advantages in addressing complex flow problems, particularly in simulating rotating flows, jet impingement, and other intricate flow scenarios, where it delivers enhanced predictive reliability (Jayakumar et al., 2010; Liu et al., 2019; Oflaz, 2025; Wang et al., 2025).

The transport equations in this model are written as:

$$\frac{\partial k}{\partial t} + \frac{\partial k u_i}{\partial x_i} = \frac{\partial}{\partial x_i}\left[D k_{eff} \frac{\partial k}{\partial x_i}\right] + G_k - \varepsilon \tag{6}$$

$$\frac{\partial \varepsilon}{\partial t} + \frac{\partial \varepsilon u_i}{\partial x_i} = \frac{\partial}{\partial x_i}\left[D \varepsilon_{eff} \frac{\partial \varepsilon}{\partial x_i}\right] + \sqrt{2} C_{1\varepsilon} S_{ij} \varepsilon - C_{2\varepsilon} \frac{\varepsilon^2}{k + \sqrt{v\varepsilon}} \tag{7}$$

with the turbulent viscosity determined by:

$$v_t = \frac{C_\mu k^2}{\varepsilon} \tag{8}$$

$$C_\mu = \frac{1}{A_0 + A_s \frac{k U^*}{\varepsilon}} \tag{9}$$

$$U^* = \sqrt{S_{ij} S_{ij} + \tilde{\Omega}_{ij} \tilde{\Omega}_{ij}} \tag{10}$$

$$\tilde{\Omega}_{ij} = \bar{\Omega} - 3\varepsilon_{ijk}\omega_k \tag{11}$$

$$A_0 = 4.04, A_s = \sqrt{6}cos\varphi \tag{12}$$

$$\varphi = \frac{1}{3} Arc\,cos\left(min\left(ma\,x\left(\sqrt{6}W, -1\right), 1\right)\right) \tag{13}$$

$$W = \frac{S_{ij}\, S_{jk}\, S_{ki}}{\tilde{S}^2} \tag{14}$$

$$C_{1\varepsilon} = \max\left(\frac{\eta}{5+\eta}, 0.43\right) \tag{15}$$

The constants C_2, σ_k, $\sigma_\varepsilon$were specified by Shih et al. (1995) and are defined as:

$$C_2 = 1.9, \sigma_k = 1.0, and\ \sigma_\varepsilon = 1.2$$

4. Results and Discussion

Figure 6 presents hydrodynamic simulations of the device's operational flow patterns under rotational conditions of 180 RPM, with jet flow parameters set to 16 m/s injection velocity and 45° nozzle orientation. Given the dominant influence of the turbulent submerged jet on global flow patterns, two orthogonal planar sections were analyzed: Section A (transverse plane aligned with jet axis) and Section B (longitudinal plane parallel to jet propagation), demonstrating device-induced modifications to the ambient flow field. Rotational

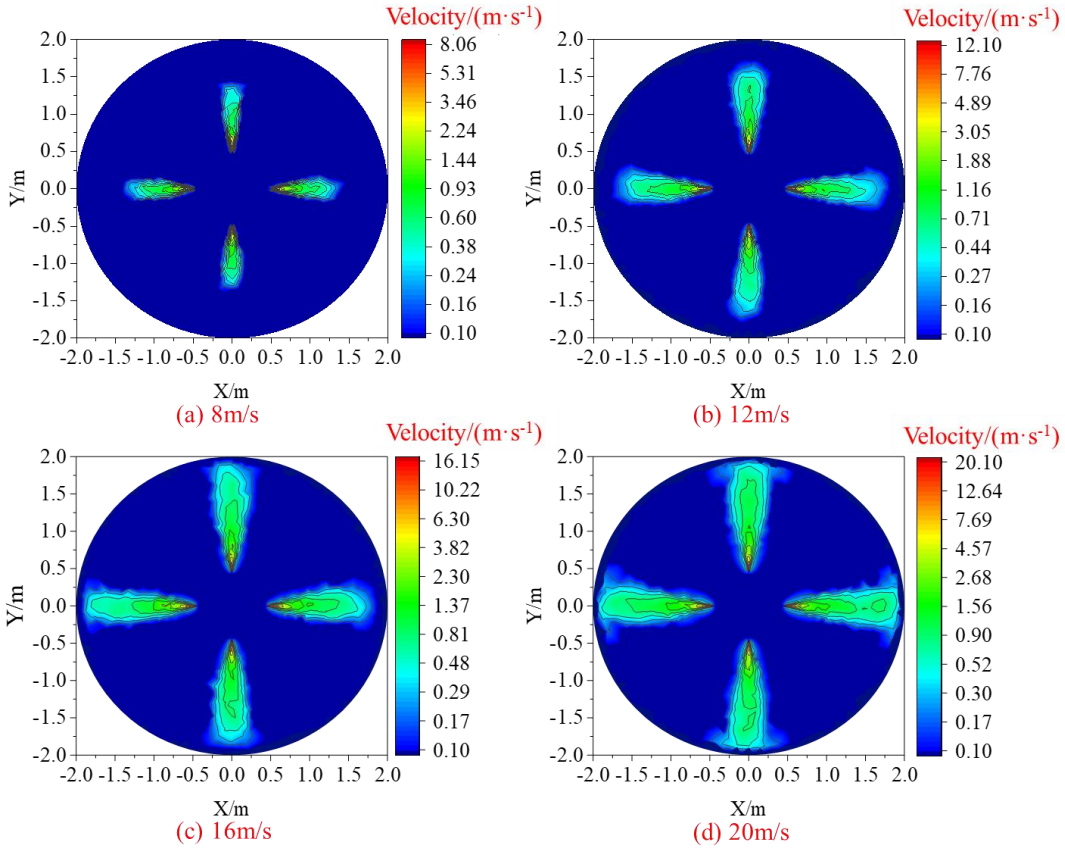

Fig. 7 Cloud map of velocity distribution in Section A for various injection velocities

operation of the tool's outer casing alters the surrounding flow dynamics, generating vortex structures through turbulent annular jet interactions.

4.1 Influence of Injection Velocity on Surrounding Flow Characteristics

Figure 7 illustrates the cross-sectional velocity distribution at various injection velocities (with a rotational speed of 0 RPM and a nozzle angle of 45°). Figures 7 a, b, c, and d correspond to injection velocities of 8 m/s, 12 m/s, 16 m/s, and 20 m/s, respectively. The selected cross-section is the Section A in Fig. 6. In aqueous salt rock leaching processes, both diffusive and convective mechanisms are present. The introduction of turbulent jets into salt caverns enhances forced convective flows, significantly accelerating solute transport rates and facilitating salt dissolution-diffusion dynamics, ultimately modifying the coupled water-salt mass transfer behavior. Under static operational conditions (0 RPM), Fig. 7 demonstrates that enhanced injection velocities induced progressive expansion of a swirling turbulent jet's spatial dimensions (reach and spread) within the submerged environment, thereby amplifying forced convective transport.

To analyze the relationship between injection velocity and turbulent circular jet axial velocity, velocity distribution graphs were generated at the jet axial line for different injection velocities, and curve fitting was performed using the ExpDecay3 model (shown in Fig. 8). When the velocity of the jet stream was reduced to 1 m/s, the jet distance was 0.9 m, 1 m, 1.24 m, and 1.28 m at an injection velocity of 8 m/s, 12 m/s, 16 m/s, and 20 m/s, respectively, indicating a positive correlation between the distance and width of the high-speed jet stream. In addition, the growth amplitudes of the jet distance and width decreased rapidly when the injection velocity exceeded 16 m/s. This is because high-velocity jets suck up the slower-flowing fluids around them and are highly prone to vortex formation. The greater the injection velocity, the greater the number of vortices, resulting in the kinetic energy of the jet decaying more rapidly in the direction of flow.

4.2. Influence of Rotational Speed on Surrounding Flow Characteristics

Velocity distribution profiles across the flow field under different rotational conditions are presented in Fig. 9. With an injection velocity of 16 m/s, the analysis focused on Section A (refer to Fig. 6 for spatial orientation).

Operational rotation of the device produced a high-velocity swirling jet, which enhanced the spatial extent of forced convective flows. As the rotational speed increased, the forced convection generated inside the cavity exhibited dynamic variations. Specifically, the maximum diameter of the convection zone progressively decreased, accompanied by a corresponding reduction in the minimum diameter, leading to a dynamic equilibrium in overall dimensions. Concurrently, the overall morphology of the convection zone evolved from a fragmented sheet-

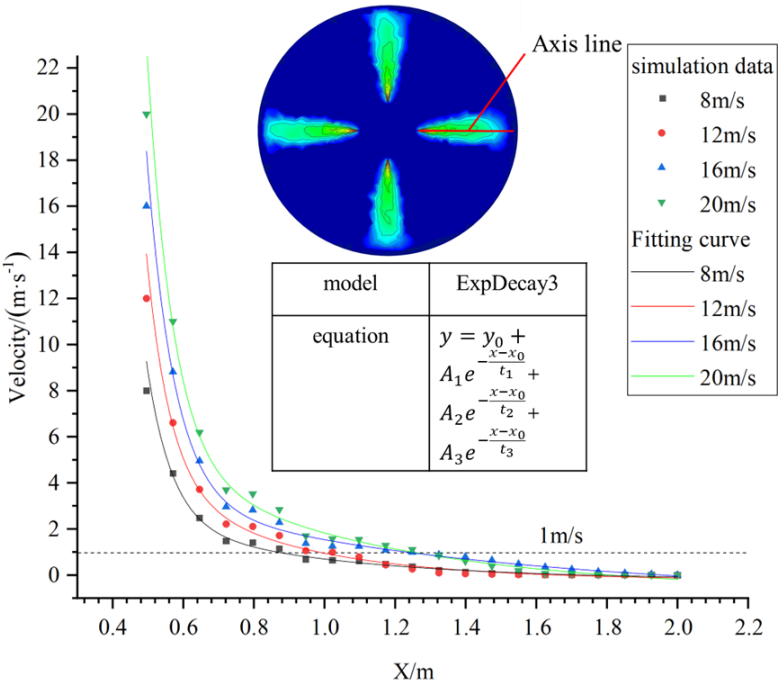

Fig. 8 Velocity distribution curves on the axial line for different injection velocities

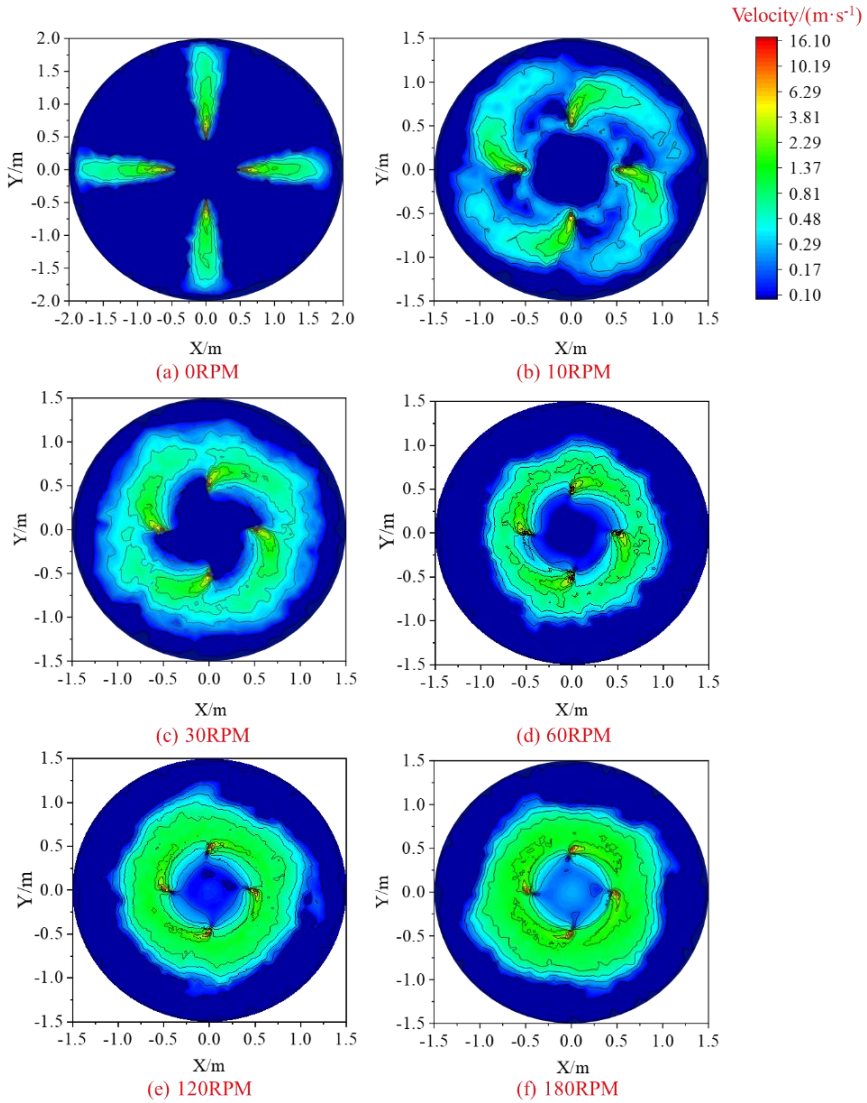

Fig. 9 Velocity distribution cloud map of different rotational speeds in Section A

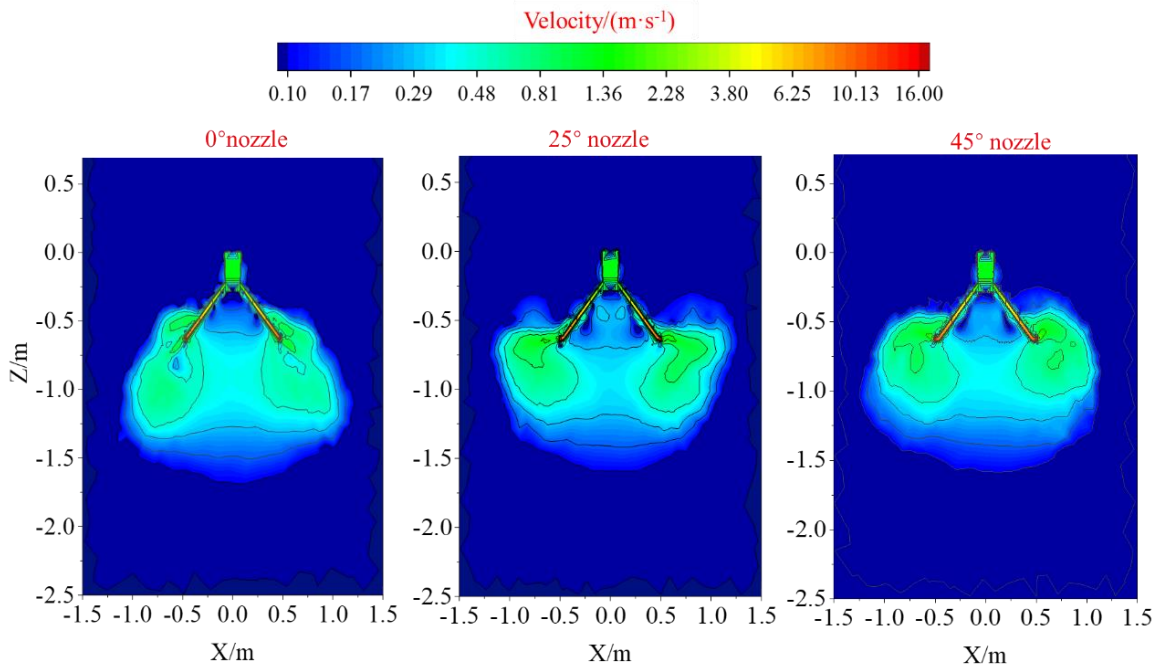

Fig. 10 Velocity distribution cloud map at Section B with varying nozzle angles

like structure to a continuous cluster-like pattern. Notably, the central region of Section A gradually transitioned into a dominant area of forced convection. This phenomenon was attributed to the enhanced centrifugal and tangential forces induced by the increased rotational speed, which redirected the high-speed jet flow from radial to circumferential motion. Consequently, each individual jet adopted a circular trajectory.

At lower rotational speeds, most of the kinetic energy decayed in a single high-speed jet due to its interaction with the surrounding quiescent fluid, whereas at higher speeds, most of the decay was caused by collisions between adjacent jets.

4.3. Influence of Nozzle Inclination Angle on Surrounding Flow Characteristics

Figure 10 illustrates the velocity cross-sectional distribution cloud map for the three nozzle angles at the same device speed (180 RPM) and injection velocity (16 m/s), with selection of the Section B from Fig. 6. As depicted in Fig. 10, the turbulent shape at 0° was conical with a smaller top and larger bottom; at 25°, it was an inverted conical shape with a larger top and smaller bottom; and at 45°, it was square. The shape of a turbulent circular jet reflects the fluid flow state, which in turn affects the size and shape of the jet that may ultimately form inside the salt cavity. Using nozzles at different angles in this device result in cavities of different shapes.

The SWV construction technique manipulated the cavity shape by altering the water circulation. Positive-circulation water dissolution is effective in creating a near-pear-shaped cavity with a larger base and smaller top, which is stable and capable of storing large amounts of sediment (Li et al. 2016, SUN et al. 2022). Reverse circulation water dissolution tends to form inverted conical cavities that are unstable and prone to collapse. The shape of the cavity can be changed using positive circulation during the trench-construction phase. In our device, turbulent flow at a nozzle angle of 0° generated a conical cavity, offering the advantage of positive circulation cavities. The turbulent flow at a nozzle angle of 25° generated an inverted conical cavity, exhibiting the disadvantages of reverse circulation cavities. Consequently, a nozzle angle of 0 °was determined as the optimal trenching angle during the trench-construction phase for our device.

5. CONCLUSIONS

This research focused on the development of a novel extendable leaching-optimized device, complemented by hydrodynamic simulations of its external flow environment. Key findings include:

(1) The extendable leaching-optimized device integrates three operational capabilities: adjustable working modes, flexible extension mechanisms, and interchangeable nozzle configurations.

(2) Higher injection velocity exhibited a direct relationship with the spatial dimensions (distance and width) of the high-speed jet, though growth rates for these parameters declined sharply beyond 16 m/s. Additionally, device rotation rates played a critical role in modulating flow behavior inside the cavern. At lower rotational speeds, the kinetic energy decay of a single high-speed turbulent circular jet was primarily due to the entrainment of the static fluid from the surrounding submerged flow. However, at higher rotational speeds, the kinetic energy decay was primarily attributed to the collision between two adjacent high-speed jet streams. Therefore, it is recommended that the device should be operated at lower rotational speeds to minimize the kinetic energy loss of individual high-speed turbulent circular jets.

(3) The nozzle inclination angle of the extendable leaching-optimized device influenced the shape of the cavity during the construction of the salt cavity storage reservoir, and the shape of the cavity can be changed using positive circulation. When using the device during trench construction, the turbulent shape formed by the 0° nozzle was conical, which is advantageous in terms of having a positive circulation cavity, good stability, low susceptibility to central pipe blockage, and the ability to accumulate a large amount of sediment at the bottom.

ACKNOWLEDGEMENTS

This research was supported by the Natural Science Foundation of China (Contract No. U23B2081).

CONFLICTS OF INTEREST

The authors of this work declare that there are no conflicts of interest.

AUTHORS CONTRIBUTION

Chunqing Zha: Validation, Resources, Supervision. **Ruihao Pang:** Conceptualization, Software, Writing – Original Draft. **Wei Wang:** Formal Analysis, Funding Acquisition, Writing – Review & Editing. **Jie Chen:** Investigation. **Jincheng Zhao:** Investigation.

REFERENCES

Albertson, M. L., Dai, Y. B., Jensen, R. A., & Rouse, H. (1950). Diffusion of submerged jets. *American Society of Civil Engineers, 115(11)*, 639-664. https://doi.org/10.2307/1990407.

Ban, F., Xiao, L., Yuan, G., & Yang, C. (2012). Rapid solution mining technology for underground gas storage in salt caverns and case histories. *Natural Gas Industry, 32 (09),* 77-79. https://doi.org/10.3787/j.issn.1000-0976.2012.09.018.

Ding, G., Li, C., Wang, J., Xu, H., Zheng, Y., Wanyan, Q., & Zhao, Y. (2015). The status quo and technical development direction of underground gas storage in China. *Natural Gas Industry, 35(11),* 107-112. https://doi.org/10.3787/j.issn.1000-0976.2015.11.017

Durie, R. W., & Jessen, F. W. (1964). Mechanism of the Dissolution of Salt in the Formation of Underground Salt Cavities. *Society of Petroleum Engineers Journal, 4(02),* 183-190. https://doi.org/10.2118/678-PA.

Jayakumar, J. S., Mahajani, S. M., Mandal, J. C., Iyer, K. N., & Vijayan, P. K. (2010). CFD analysis of single-phase flows inside helically coiled tubes. *Computers & Chemical Engineering, 34(04),* 430-446, https://doi.org/10.1016/j.compchemeng.2009.11.008.

Jiang, D., Li, X., Chen, J., Li, X., Liu, W., & Kang, Y. (2019). Model test and numerical calculation of double-well flow field in layered salt rock. *Rock and Soil Mechanics, 40*(1), 165-172. https://doi.org/10.16285/j.rsm.2017.0960

Jiang, D., Wang, C., Ren, S., & Chen, J. (2012). Experiments of the influencing factors on dissolution rate of rock salt. *Journal of Chongqing University, 35*(09), 126-130. https://doi.org/10.11835/j.issn.1000-582X.2012.09.019.

Jiang, D., Yi, L., Chen, J., Ren, S., & Li, Y. (2016). Comparison of cavern formation in massive salt blocks with single-well and two-well systems, *Journal of the Chinese Institute of Engineers, 39*(8), 954–961. https://doi.org/10.1080/02533839.2016.1220266.

Li, J., Yang, C., Shi, X., Xu, W., Li, Y., & Daemen, J. (2020). Construction modeling and shape prediction of horizontal salt caverns for gas/oil storage in bedded salt. *Journal of Petroleum Science and Engineering, 190*, 107058. https://doi.org/10.1016/j.petrol.2020.107058.

Li, L., Hou, L., Li, J., Fan, L., Li, X., Li, H., & Wang, G. (2023). Influence of well spacing on solution mining of small-spacing dual well in salt cavern gas storages. *Oil & Gas Storage and Transportation, 42*(7), 826-834. https://doi.org/10.6047/j.issn.10008241.2023.07.012.

Li, X. (2016). The construction technology of salt cavern gas storage. *Contemporary Chemical Industry, 45*(07), 1460-1463. https://doi.org/10.13840/j.cnki.cn211457/tq.2016.07.041

Liu, W., Jiang, D., Chen, J., Daemen, J., & Wu, F. (2017). Comprehensive feasibility study of two-well-horizontal caverns for natural gas storage in thinly-bedded salt rocks in China. *Energy, 143* (15), 1006–1019. https://doi.org/10.1016/j. energy.2017.10.126.

Liu, X., Yang, X., Zhong, Z., Liang, N., Wang, J., & Huang, M. (2015). Research on dynamic dissolving model and experiment for rock salt under different flow conditions. *Advances in Materials Science & Engineering,* 1-10. https://doi.org/10.1155/2015/959726.

Liu, Z., Yue, Y., She, L., & Fan, G. (2019). Numerical analysis of turbulent flow and heat transfer in internally finned tubes. *Frontiers in Energy Research 7*, 64. https://doi.org/10.3389/fenrg.2019.00064.

Moditis, K., Paidoussis, M., & Ratigan, J. (2016). Dynamics of a partially confined, discharging, cantilever pipe with reverse external flow. *Journal of Fluids and Structures, 63,* 120–139. https://doi.org/10.1016/j.jfluidstructs.2016.03.002.

Niu, C. K., Tan, Y. F., Li, J. N., & Song, C. L. (2015). Model validation and stability analysis for operation projects in Jintan Salt Cavern for strategic oil storage of China. *Journal of Petroleum Science and*

Engineering. 127, 44–52. https://doi.org/10.1016/j.petrol.2015.01.029

Oflaz, F. (2025). Evaluation of the thermo-hydraulic behavior of water-based graphene and Al2O3 hybrid nanofluids in a circular tube through CFD simulations. *Journal of Thermal Analysis and Calorimetry,* https://doi.org/10.1007/s10973-025-13993-4.

Shaheed, R., Mohammadian, A., & Kheirkhah Gildeh, H. (2019). A comparison of standard k–ε and realizable k–ε turbulence models in curved and confluent channels. *Environmental Fluid Mechanics 19,* 543–568. https://doi.org/10.1007/s10652-018-9637-1.

Shi, X. L., Li, Y. P., Yang, C. H., Xu, Y. L., Ma, H. L., Liu, W., & Ji, G. D. (2015). Influences of filling abandoned salt caverns with alkali wastes on surface subsidence. *Environmental Earth Sciences, 73,* 6939–6950. https://doi.org/10.1007/s12665-015-4135-y

Shih, T. H., Zhu, J., & Lumley, J. L. (1995). A new Reynolds stress algebraic equation model. *Computer Methods in Applied Mechanics and Engineering, 125,* 287-302, https://doi.org/10.1016/0045-7825(95)00796-4.

Stiller, M., Yechieli, Y., & Gavrieli, I. (2016). Rates of halite dissolution in natural brines: Dead Sea solutions as a case study. *Chemical Geology, 447,* 161-172. https://doi.org/10.1016/j.chemgeo.2016.10.023

Sun, J., Chen, J., Jing, G., Yang, P., Wang, Y., & Meng, J. (2022). Research progress on key technologies of salt cavern gas storage construction in china. *Salt Science and Chemical Industry, 51*(10), 1-7. https://doi.org/10.16570/j.cnki.issn16736850.2022.10.001

Wang, J., Wang, Z., Zeng, Q., Ding, G., Li, K., Wanyan, Q., & Wang, Y. (2023). Simulation of flow field of solution mining salt cavities for underground gas storage. *Journal of Energy Resources Technology, 145*(2), 022001. https://doi.org/10.1115/1.4054913

Wang, R., Wang, Y., Wang, M., Wang, Z., & Chen, X. (2025). Research on the influence of turbulence models on numerical simulation results of cross wavy heat exchanger channels. *International Communications in Heat and Mass Transfer, 161,* 108461, https://doi.org/10.1016/j.icheatmasstransfer.2024.108461.

Yang, C., Wang, T., Li, Y., Yang, H., Li, J., Qu, D., Xu, B., Yang, Y., & Daemen, J. (2015). Feasibility analysis of using abandoned salt caverns for largescale underground energy storage in China. *Applied Energy, 137* (1), 467–481. https://doi.org/10.1016/j.apenergy.2014.07.048.

Yang, X., Liu, X., Zang, W., Lin, Z., & Wang, Q. (2017). A study of analytical solution for the special dissolution rate model of rock salt. *Advances in Materials Science and Engineering, 2017*(4), 1-8. https://doi.org/10.1155/2017/4967913

Yuan, G., Shen, R., Tian, Z., & Yuan, J. (2006). Research and field application of quick speed solution mining technology. *Journal of Petroleum,* 139-142. https://doi.org/10.3321/j.issn:02532697.2006.04.031 .

Yuan, G., Wan, J., Li, J., Li, G., Xia, Y., Ban, F., Zhang, H., Jurado, M. J., Peng, T., & Liu, W. (2021). Stability analysis of a typical two-well-horizontal saddle-shaped salt cavern. *Energy Storage, 40,* 102763. https://doi.org/10.1016/j.est.2021.102763

Zhang, J., Jiang, D., Chen, J., Zhao, Y., & Cheng, Y. (2017). Effect of brine flux on damage and dissolving characteristics of rock salt under the condition of complex stress unloading. *Rock and Soil Mechanics, 38*(03), 640-655. https://doi.org/10.16285/j.rsm.2017.03.004.

Zhang, T., Wang, X., Hu, J., Ye, J., Wu, Y., & Wen, X. (2022). Experimental study on erosion characteristics of salt rock by water jet under low pressure. *Journal of Energy Storage, 55,* Part C. https://doi.org/j.est.2022.105690.

Zhao, Z., Zhu, W., Shan, W., & Wan, Y. (2003). Research on mechanism of solution mining for building underground gas storage in salt cavern. *Petroleum Exploration and Development,* 107-109. https://doi.org/10.3321/j.issn:10000747.2003.05.032 .

Zong, S., Liu, S., Xu, H., Wang, W., Cao, B., & Huang, F. (2023). Numerical simulation of CO2 storage in bedded salt rock storage cavern in Subei Basin. *Coal Geology and Exploration,* 27-36. https://doi.org/10.12363/issn.1001-1986.22.09.0666